A quantitative multi-parameter mapping protocol standardized for clinical research in autoimmune neuroinflammatory diseases with white matter abnormalities

Keywords: quantitative MRI, multi-parameter mapping, neuroimaging, multiple sclerosis, aging, proton density

Henri Trang[1,2#], MS, Tim J. Hartung[3#], MD, Qianlan Chen[1], MD, Stefan Hetzer[4], PhD , Claudia Chien[1,5,6], PhD, Pia S. Sperber[1,2,6], MD, Tanja Schmitz-Hübsch[1,2,6], MD, Susanna Asseyer[1,2,3,6], MD, Rebekka Rust[1,6,7], MD , Darius Mewes[1,8,], Lina Anderhalten[1,2,6], MD, Michael Sy[9], MD, PhD, Alexander U. Brandt[1,9#], MD, Carsten Finke[3*], MD, Friedemann Paul[1,2,3,6*], MD

1) Experimental and Clinical Research Center, a cooperation between Max Delbrück Center for Molecular Medicine in the Helmholtz Association and Charité – Universitätsmedizin Berlin, Berlin, Germany.
2) Max Delbrück Center for Molecular Medicine in the Helmholtz Association (MDC), Berlin, Germany.
3) Charité – Universitätsmedizin Berlin, corporate member of Freie Universität Berlin and Humboldt-Universität zu Berlin, Department of Neurology and Experimental Neurology, Berlin, Germany
4) Berlin Center for Advanced Neuroimaging, Charité – Universitätsmedizin Berlin, corporate member of Freie Universität Berlin, Humboldt-Universität zu Berlin, and Berlin Institute of Health, Berlin, Germany

5) Charité – Universitätsmedizin Berlin, corporate member of Freie Universität Berlin and Humboldt-Universität zu Berlin, and Berlin Institute of Health, Department of Psychiatry and Neurosciences, Berlin, Germany

6) NCRC – Neuroscience Clinical Research Center, Charité – Universitätsmedizin Berlin, Berlin, Germany

7) Institut für Med. Immunologie, Immundefektambulanz, Charité – Universitätsmedizin Berlin, Germany

8) Berlin Institute of Health at Charité – Universitätsmedizin Berlin, Biomedical Innovation Academy, Berlin, Germany

9) Department of Neurology, University of California Irvine, 208 Sprague Hall, Mail Code 4032, Irvine, CA 92697, USA

[#] **co-first authors**

*** corresponding authors**

friedemann.paul@charite.de

Phone: +49 30 450 539 705 Fax: +49 30 450 539 915

Address: Charité – Universitätsmedizin Berlin, Geschäftsführung, Charitéplatz 1, 10117 Berlin

carsten.finke@charite.de

Phone: +49 30 450 560 216 Fax: +49 30 450 560 901

Address: Charité – Universitätsmedizin Berlin, Augustenburger Platz 1, 13353 Berlin

Abstract

Quantitative magnetic resonance imaging (qMRI) involves mapping microstructure in standardized units sensitive to histological properties and supplements conventional MRI, which relies on contrast weighted images where intensities have no biophysical meaning. While measuring tissue properties such as myelin, iron or water content is desired in a disease context, qMRI changes may typically reflect mixed influences from aging or pre-clinical degeneration. We used a fast multi-parameter mapping (MPM) protocol for clinical routine at 3T to reconstruct whole-brain quantitative maps of magnetization transfer saturation (MT), proton density (PD), longitudinal (R1), and transverse relaxation rate (R2*) with 1.6 mm isotropic resolution. We report reference MPM values from a healthy population with age and gender distributions typical of neuroimmunology studies in whole brain white matter (WM), T2-weighted WM hyperintensities, cortical grey matter and deep grey matter regions and present post-processing optimizations including integration of lesions and normalization of PD maps against cerebrospinal fluid (CSF) for standardized research in multiple sclerosis (MS) and related disorders. PD maps were affected by WM abnormalities in MS using WM calibration. The results acknowledge the impact of non-linear age effects on MPM and suggest using

CSF calibration for future clinical application in autoimmune neuroinflammatory diseases with WM abnormalities.

1 Introduction

Quantitative magnetic resonance imaging involves mapping microstructure in standardized physical units containing information about the local tissue environment surrounding the protons, thereby enhancing comparability in time and space. Quantitative maps supplement conventional MRI, which relies on contrast weighted images where intensities have no biophysical meaning, in providing insight into biologically meaningful microstructural properties of the central nervous system at the mesoscopic scale [1,2]. Research in quantitative relaxometry and magnetization transfer imaging has shown strong reproducibility and sensitivity, exhibiting a robust correlation with histological measurements and accepted metrics related to water [3], myelin [4], and iron content [5].

Standardized scanning protocols at 3T and tools to reconstruct parametric maps demonstrating multi-center reproducibility are readily available [6,7] such as the time-efficient multi-parameter mapping (MPM) protocol [6] consisting of 3D multi-echo fast low angle shot (FLASH) acquisitions. It allows for estimation of quantitative maps of proton density (PD), magnetization transfer saturation (MT), longitudinal relaxation rate (R1=1/T1), and effective transverse relaxation rate ($R2^*=1/T2^*$) facilitated by the open-source 'hMRI toolbox' [8], which includes spatial processing tailored for voxel-wise statistical analysis of quantitative cerebral MRI data.

Several studies have collected quantitative relaxometry, MT and PD maps of healthy brain tissue using the MPM protocol to obtain normative reference values [7,9]. These studies highlighted the influence of normal aging on brain microstructure in previous quantitative MRI studies [10,11].

This study aimed to optimize the post-processing of a previously described MPM protocol based on standard manufacturer sequences with 1.6 mm isotropic voxel resolution [12] for disease-related research, i.e. autoimmune neuroinflammatory diseases with white matter lesions such as multiple sclerosis (MS) or neuromyelitis optica spectrum disorder (NMOSD). MS and NMOSD are immune-mediated inflammatory diseases of the central nervous system with overlapping clinical characteristics shown to predominantly affect women, given a markedly high female to male ratio in MS[13] and NMOSD[14]. In a large healthy cohort with a gender distribution typical of neuroimmunology studies, we established reference values of MT, R1, PD and R2* in white matter (WM), T2-weighted (T2w) WM hyperintensities, cortical grey matter (CGM) and deep gray matter (DGM) regions. We compared WM and T2w WM hyperintensities values across MS patients and healthy controls. We standardized PD maps using reference values for water in cerebrospinal fluid (CSF) of the lateral ventricles [15] and compared them to maps scaled to 69% in WM to highlight the impact of focal and diffuse white matter damage between MS patients and healthy controls. We further evaluated MPM-derived parameters and their associations with age and sex to inform future studies that may require strategies to correct for confounding effects of these factors when using MPM in clinical research.

92

93 ## 2 Materials and Methods

94 ### 2.1 Subjects

95 #### 2.1.1 Informed Consent

96 The analysis was performed as part of the BERLimmun [16] (EA1/362/20, DRKS00026761), ViMS [17]
97 (EA1/182/10) and CAMINO [18] (EA2/007/21) neuroimmunology studies, approved by the
98 institutional ethics committee of our institution and conducted in accordance with the Declaration of
99 Helsinki in its applicable version for the conduction of the study. All participants gave written
100 informed consent.

101 #### 2.1.2 Study Population

102 Demographics are summarized in Table 1. From April 2015 to September 2022, we pooled healthy
103 participants recruited from the 3 previous separate registries. For the control group, participants
104 without history of neurological or psychiatric disorders (and without previous COVID-19 infection
105 for the CAMINO cohort) were recruited in Germany. Additional inclusion criteria were the
106 following: self-declared healthy, older than 18 years of age, an active health insurance, competent to
107 give written informed consent. Exclusion criteria consisted of contraindication to MRI investigation
108 at inclusion, pregnancy, disease hindering the conduct of the study or inability to cooperate. Initially,
109 we collected scans from 78 healthy participants. We excluded one participant from analyses because

scans were of poor image quality. In total 77 healthy controls, 60 (77.9%) women and 17 (22.1%) men, with age ranging from 20 to 75 years, with a mean [±standard deviation (SD)] of 42.1 ± 14.1 years, were included (14 from BERLimmun, 14 from ViMS, 49 from CAMINO). Additionally, 27 patients diagnosed with MS (18 women (67%), mean age 50 ± 9.9 years) were included from the ViMS study according to the revised McDonald diagnosis criteria [19].

2.2 MRI

2.2.1 Acquisition

MRI scans were acquired on a single 3T MR scanner (Magnetom Prisma, Siemens Healthineers, Erlangen, Germany) using a 64-channel receive radiofrequency (RF) head-neck coil covering brain and cervical spinal cord. To maintain reproducibility across participants and time points, the acquisition protocol, and participant positioning remained identical to that detailed in a prior study, aside from updating the head coil [12]. Briefly, the MPM sequence is 7 minutes in length, 1.6 mm isotropic resolution with three distinct 3D multi-echo fast low-angle shot (FLASH) gradient-echo acquisitions. For post-acquisition bias-field correction, a radiofrequency (RF) transmit (B1+) map was acquired during each session with an isotropic resolution of 4 mm from spin-echo/stimulated echo acquisitions utilizing a standard vendor sequence [7]. MT-weighting was achieved by applying an off-resonance Gaussian pulse (500°, 10 ms, 1,200 Hz off-resonance, 192 Hz bandwidth) prior to non-selective excitation. In addition, the BERLimmun scan protocol included a structural T1-weighted

(T1w) scan (3D MPRAGE, TR=1,900 ms, TE=2.55 ms, TI=900 ms, 0.8 mm isotropic resolution) and T2w fluid-attenuated inversion recovery (3D FLAIR, TR=6,000 ms, TE=388 ms, TI=2,100 ms, 0.8 mm isotropic resolution). The CAMINO scan protocol included a 3D-MPRAGE (1 mm isotropic resolution, TR=1900 ms, TE=2.22 ms, TI=2100 ms).

2.2.2 Quantitative map reconstruction

We generated quantitative PD, MT, R1, and $R2^*$ maps utilizing MATLAB (MathWorks) with the hMRI toolbox [8] implemented within SPM12 (http://www.fil.ion.ucl.ac.uk/spm/software/spm12/). These maps were reconstructed given the PD-weighted (PDw), MT-weighted (MTw), and T1w echoes acquired through FLASH acquisitions and corrected for transmit and receive field inhomogeneities [20]. Correction of Gibbs ringing artifacts [21] was performed prior to reconstruction of the quantitative maps, consisting in the removal of oscillatory patterns situated around tissue borders from all six echoes of the raw images (PDw, MTw, T1w). Motion degradation index for each of the raw averaged echo images (PDw, MTw, T1w) were obtained from the toolbox to identify scans with motion artifacts [22]. Correlation of motion degradation index with age was assessed to evaluate the impact of motion on $R2^*$ variability with age (Sup. Fig. S1). Finally, given the use of an off-saturation MT pulse with a flip angle of 500°, we linearly rescaled MT maps to harmonize values for comparison to literature values obtained with a 220° flip angle, as recent evidence showed that a linear rescaling to harmonize MT maps across manufacturers effectively reduced the inter-site bias [7].

2.2.3 Post-processing

T1-MPRAGE and T2-FLAIR images underwent bias-field correction using non-parametric non-uniform intensity normalization [23] and were subsequently reoriented to the Montreal Neurological Institute (MNI) standard reference space for further lesion delineation using FSL FLIRT (http://www.fmrib.ox.ac.uk/fsl).

2.2.4 Segmentation

Two expert MRI technicians (15-17 years of experience) performed manual segmentation using ITK-SNAP (available at www.itksnap.org) of T2w hyperintense brain lesions on FLAIR images linearly co-registered to MPRAGE images [24]. We subsequently refer to our segmentations as WM lesions (WML), rather than the general T2w-hyperintensities. We only included lesion masks with a WML mean volume above a pragmatic cutoff of 0.20 mL, corresponding to a Fazekas visual rating score of 1 [25,26]. Generation of a brain mask and tissue segmentation of T1-MPRAGE images to obtain WM, CGM and DGM masks were achieved via FastSurfer [27]. Lesion-filled WM masks were obtained by subtracting lesions from WM masks. Additionally, for each mask, voxels with T1 values higher than 4s within the tissue masks were removed for further correction of partial volume effect [28]. All masks and structural images were then linearly co-registered via FSL FLIRT to native space using the T1w image as reference. Median parameter values were extracted from WM, CGM and several atlas-defined deep grey matter structures (thalamus, caudate nucleus, putamen, globus pallidus,

164 hippocampus, amygdala, and nucleus accumbens) for each participant with both hemispheres
165 summed.

166 **2.2.5 PD calibration**

167 The PD map output from the hMRI toolbox was corrected for $R2^*$ by extrapolating the signal at
168 TE=0ms and was originally calibrated as 69% water content in the WM [8]. To demonstrate bias
169 resulting from WM abnormalities in MS patients, PD maps calibrated using a whole WM mask and a
170 lesion-filled WM mask were compared respectively in the whole WM region (including WML) and
171 the normal appearing WM region free of WML (NAWM).

172 Subsequently, reconstructed PD maps from the hMRI toolbox were recalibrated as pure water (100 %
173 reference) based on the median CSF signal in the lateral ventricles[28], using a mask from the Harvard
174 Oxford template distributed with FSL (Functional MRI of the Brain Software Library,
175 http://www.fmrib.ox.ac.uk/fsl/) warped into subject native space. To reduce partial volume effects,
176 lateral ventricles masks were eroded by 1 voxel then corrected by multiplying them with a CSF tissue
177 mask obtained from the respective tissue probability map (threshold of 0.9). Finally, we excluded
178 voxels with T1 values lower than 4s to obtain only voxels with pure water in CSF, based on the
179 quantitative R1 map output from the reconstruction toolbox. To account for a potential bias
180 introduced by CSF volume or T1 variability in CSF, we compared our method to a calibration
181 selecting only the 100 voxels with the shortest T1 times above the 4s cutoff, therefore obtaining a

182 mask with the same volume across participants over voxels with a small range of T1 above 4s. We
183 calculated coefficients of variation (CoV) of the scaling factor, which is the multiplication factor
184 obtained to scale each individual PD map by dividing 100 % by its respective median in CSF.

185 **2.3 Statistical Analyses**

186 **2.3.1.1 Descriptive statistics**

187 Histogram analysis of brain tissues was first done to assess distribution of the entire dataset in WM,
188 WML, CGM and DGM (Sup. Fig. S2). To get a better representation of a healthy population cross-
189 sectional data for each brain region of interest (ROI), all subsequent analyses were performed on data
190 free from respective outliers outside the ROI-specific 2^{nd}-98^{th} percentile. Statistical analysis was
191 conducted in R (R Core Team, https://www.r-project.org). Normality of data distribution was tested
192 using a Shapiro-Wilk test. Median MPM metrics in each brain ROI were used for statistical analysis.
193 Structural volume of the considered ROI was normalized by intracranial volume to obtain an adjusted
194 volume and account for intracranial volume differences between men and women. Differences
195 between WM and WML across MS patients and healthy controls were assessed using ANOVA and
196 linear regression models adjusted for age and sex followed by post-hoc Tukey tests.

197 **2.3.1.2 Sex differences**

198 Interaction between sex and age was tested before excluding the former variable as a possible
199 covariate for MPM-derived parameters. Analysis of sex on median MPM parameter showed no

200 difference between men and women, including normalized structure volume as an additional
201 covariate in the linear regression model. Therefore, all regression models were fitted non-stratified,
202 i.e. by combining data from both men and women.

203 **2.3.1.3 MPM age effects**

204 For the assessment of the relationship between MPM-derived parameters and age, MS subjects were
205 excluded. Linear and non-linear relationships between each MPM parameter and age were tested for
206 every structure. A polynomial regression model was built for each tissue parameter with age, adding
207 normalized volume and sex as covariables. Orthogonal polynomials were used to reduce
208 multicollinearity effects of age predictors (e.g. covariance of age, age^2, age^3). This was implemented
209 in R using the "poly()" function from the "stats" package. Non-linear volume dependency with age
210 was further assessed by exploring the significance of the quadratic term.

211 Additionally, visual inspection of MPM-by-age scatterplots with LOESS-fitted trend lines indicated
212 that a 1-knot linear spline model could best fit the age-related distribution. We selected a cutoff of 55
213 years (≥55) for the spline, which represented a split at approximately the 80th quantile. This is
214 consistent with the upper age limit of most clinical drug trials in multiple sclerosis, as the
215 confounding effect of vascular lesions and other comorbidities increases beyond this cut-off.
216 Furthermore, diffusion tensor imaging studies revealed that age-related decline is more apparent in
217 the fifth decade of life [29].

2.3.1.4 Model selection

We compared the performance of linear, linear spline, quadratic, cubic and exponential models to choose the simplest best fitting model according to a likelihood ratio test in addition to Akaike information criterion (AIC) comparison. The simplest model was generally chosen when the likelihood ratio-test did not return a significant difference.

3 Results

3.1 PD calibration

We chose to standardize PD based on ventricular CSF (see Fig.1 for an illustration of the pipeline), since calibration methods using lesion-filled WM masks and whole WM masks in 27 MS patients resulted in different PD values in NAWM and WM (Fig.2a). In contrast, no difference was found between NAWM and WM in effective PD (without calibration) or when using CSF as reference (Fig.2b and 2c).

Lateral ventricles masks had a median volume of 5685(7934) [median(IQR)] voxels or 23.3(32.5) mL. Exclusion of voxels with a T1 below 4s resulted in a median mask volume of 2683(4596) voxels or 10.99(18.82) mL. The average percentage of voxels remaining above this T1 threshold was 44.31% (mask voxel number ranging from 262 to 31396) with a range of T1 times from 4 to 13.4s. Median T1 across participants was 5.4s in this CSF mask. CoV of the scaling factor using CSF were

236 1.51%, 0.74% and 2.38% for respective T1 thresholds at 3s, 4s and 5s, compared to 37.79% for the
237 calibration using WM. Using only the first 100 voxels with T1>4s in the mask resulted in a CoV of
238 the scaling factor of 2.20%. Normalized lateral ventricles volume was correlated with age and scaling
239 factor for the calibration using CSF, as well as scaling factor with age. However, there was no
240 association between PD in the lateral ventricles and age (Sup. Fig. S3). After normalization with the
241 CSF signal, mean intra-subject CoV of PD was 5.2 ± 0.33% in WM, 8.26 ± 0.58% in CGM and 4.84
242 ± 0.48% in DGM. Intra-subject variability remained identical to the WM-based calibration due to the
243 linear rescaling of effective PD. SD of PD across subjects were higher in WM (1.27 vs 0.17), CGM
244 (1.10 vs 0.68) and DGM (1.19 vs 0.69) with the normalization to CSF compared to calibration of PD
245 against WM resulting in higher inter-subject CoV in WM (1.82% vs 0.24%), in CGM (1.40% vs
246 0.86%) and in DGM (1.54% vs 0.88%).

247 **3.2 Healthy cohort reference values**

248 Table 2 presents descriptive statistics of MPM measurements in WM, WML, CGM, DGM, thalamus,
249 hippocampus and CSF. Data for caudate nucleus, putamen, globus pallidus, amygdala, nucleus
250 accumbens are presented in Sup. Tables S1-2. Reported mean or median values across ROIs are in
251 line with those reported in previous studies (Sup. Table S2).

252 Histograms (Fig.3) show clearly distinct peaks and normal distributions of MPM median values for
253 WM, WML, CGM and DGM. Detailed distribution density of median parameter values in DGM

254 structures is shown in Figure 4a. The pallidum stands out among the deep grey matter structures with
255 higher MT, R1 and $R2^*$ and lower PD (Fig.4a). This is further illustrated in Figure 4b displaying a
256 brain slice sampled from each population averaged parameter map.

257 **3.3 White matter lesions**

258 Fifty-two out of 77 healthy participants (67.5%) had at least one T2w WMH segmented as lesion
259 (single lesion volume > 0.01 mL) and 20 (26%) participants (mean age 50.5±14y, 6 (30% male)) had
260 a mean WML volume above the pre-defined cutoff of 0.2 mL. Mean (SD) number of lesions was
261 41.9 (46.6) and mean WML volume was 1.39 (1.63) mL (Table 1 and 2). MPM metrics and lesion
262 volume scatterplots against age are shown in Sup. Fig. S4.

263 In healthy participants, compared to normal appearing WM, MPM values in WML were significantly
264 reduced for MT (t=-7.53, 95% CI =[-0.43, -0.24], $p < 0.001$), R1 (t=-5.83, 95% CI =[-0.14, -0.07], p
265 < 0.001) and $R2^*$(t=-8.05, 95% CI =[-3.56, -2.09], $p < 0.001$) and significantly increased for PD
266 (t=5.51, 95% CI =[2.31, 5.12], $p < 0.001$). In addition, WML showed a substantially wider range of
267 MPM values across all parameters, compared to healthy WM (Fig.3).

268 MS patients had a mean T2w WMH volume of 21.5 (12.2) mL ranging from 10.3 mL to 58.2 mL
269 across patients and a mean number of lesions of 86.8 (53.7). MS-WML had increased PD and
270 reduced MT, R1 and R2* compared to MS-NAWM, HC-WM and HC-WML (Fig.3b).

271 **3.4 MPM age related changes**

As part of our objective to explore the impact of brain aging on the quantitative maps, Table 3 compiles effect sizes from the regression models, including 95% confidence intervals. Only models revealing a significant association between parameter and age in WM, CGM, DGM, thalamus and hippocampus are presented in Table 3 and outcomes of model selection are summarized in Sup. Fig. S5. For data visualization, scatterplots with the trajectory of the curve fitting in the various ROIs are attached in Fig.5 and Sup. Fig. S6.

Regression of MT, R1 and $R2^*$ showed a non-linear association with age in the quadratic term in both WM and CGM. In the thalamus, fitting MT and R1 with a quadratic function against age showed significant association, both described by a slow increase from 20 to 40y followed by a decline after 50y. In the hippocampus only R1 presented a quadratic evolution with age indicating a slow increase from 20 to 50y followed by a decline after 60y.

In WM, a linear spline performed better than a quadratic fit in explaining changes in MT and $R2^*$ with age. Summarizing the results of the model selection in WM (Table 3), MT showed an average decrease of -0.154%/year ($p < 0.001$) after 55y, $R2^*$ a decrease of $-0.648 s^{-1}$/year ($p < 0.001$) after 55y and PD increased linearly by 0.033%/year ($p=0.002$). R1 revealed a quadratic association with age ($p=0.005$) with a slow increase over 20-40y followed by a decline after 50y. Remarkably, there was no age association in both MT and $R2^*$ in WM between 20y and 55y.

In CGM, selected models were quadratic for MT, R1 and $R2^*$ and linear for PD. In the thalamus, a quadratic fit was selected for MT and R1 and in the hippocampus R1 also showed a quadratic trajectory with age.

Finally, there was no non-linear volume dependency with age across ROIs when testing the quadratic term, although correlation was present (Sup. Table S3).

4 Discussion

In this study we present an acquisition and post-processing protocol for a fast quantitative multi-parameter mapping of the brain with inclusion of T2w white matter hyperintensities and calibration of proton density using CSF. We standardize the reconstructed quantitative maps for future clinical application in demyelinating diseases and recommend calibrating PD maps as pure water in CSF to avoid bias introduced by pathology. We report reference MPM brain data for 77 healthy subjects of Caucasian ethnicity aged between 20 and 75 years and discuss age-dependence of the MPM parameters.

4.1 PD calibration

PD maps using the standard approach from the hMRI toolbox reconstruction are calibrated to 69% in WM which may lead to an underestimation of its reported variability [7]. In addition, pathologic changes of PD in WM may not be reflected, especially when considering its possible use in diseases

306 with WM abnormalities, e.g. multiple sclerosis. Using CSF-based calibration avoids these problems,
307 as CSF does not contain relevant amounts of macromolecules or paramagnetic ions and the magnetic
308 properties of CSF are largely unaffected by most neurological disorders [30].

309 We found that both diffuse and focal WM abnormalities affected the WM-based calibration. On one
310 hand, focal lesions led to a slight underestimation of PD values. On the other hand, diffuse WM
311 damage might also impact the calibration resulting in slight PD differences (~0.1-0.2 p.u) between
312 NAWM and WM while there was no difference in effective PD or when using CSF as reference. In
313 such a ROI analysis, the impact from WM lesions may be occulted by the relative volume difference
314 to whole white matter across patients. However, at the single subject level, their effect may be
315 amplified. Therefore, we recalibrated PD as 100% in CSF, so that inter-subject variability in CSF
316 would be negligible [28]. To ensure that calibration is only based on voxels containing CSF and to
317 avoid partial volume effects, we excluded voxels with T1 lower than 4s from the ventricle masks,
318 which is an appropriate threshold given that the model estimated T1 of free water in brain tissue is
319 3.7s [31]. Although T1 of CSF is known to be independent of field strength [32], reported values in
320 literature show some variability ranging from 4s to 5s. The CoV of the scaling factor did not vary
321 substantially between the usage of different T1 cut-offs from 3s to 5s. It was dramatically lower
322 using CSF (0.74% vs 37.79%). We effectively scale all voxels based on the assumption that CSF has
323 the highest water fraction. One could either assume that the highest water fractions might be capped

by the maximum intensity measured by the scanner or that biological variability in CSF is of lower order of magnitude.

Inter-subject variability is higher than in a previous study which used the conventional WM-based calibration, while intra-subject CoV is in the same order of magnitude [12]. However, our current sample has a wider age range (42.1±14.1 vs 35±7y) than the study by Cooper and colleagues. Given the variability of ventricles sizes, the resulting inter-subject CoV is higher compared to normalization to a larger homogeneous WM region. Nonetheless, taking into consideration the variation in ventricular volume in the linear models, both linear association of PD with age and CoV remained similar whether we used the ventricles mask or a fixed set of 100 voxels within it. Although correlation exists between ventricular volume and age, as well as between ventricular volume and scaling factor, the scaling factor was not correlated to age. This means that although age variability in ventricular volume introduces variability in the PD scaling factor, the resulting inter-subject variability remains low compared to inter-subject variability from WM. An alternative approach would be to obtain a scaling factor with the use of an external reference such as a phantom to benefit from a stable and homogeneous volume [33]. However, due to a lack of practicality, it is hardly considered for use in a clinical setting.

Finally, PD quantification methods may differ on the determination of the receiver sensitivity profile and values reported here are standardized for the method of quantitative B1 mapping [34]. Volz et al.

342 pointed out that physiological bias might be smoothed out and recommended to proceed carefully in
343 the presence of pathology which may cause segmentation algorithms to fail or wherein the
344 relationship between T1 and effective PD may be locally distorted [15].

345 **4.2 Age-related effects**

346 We observed a non-linear age dependency of MT, R1 and $R2^*$ across various ROIs. Age effects
347 could be best modelled linearly for PD and we found arguably a reduced impact of non-linear effects
348 between 20y and 55y for both MT and $R2^*$ in WM. Our findings corroborate MPM studies on brain
349 aging which reported negative correlation between age and MT across the cortex along positive
350 correlations between age and $R2^*$ in the basal ganglia [9-11,35].

351 A quadratic model provided the most accurate representation of the non-linear relationship between
352 MT and age, illustrating the U-shaped pattern in myelination over lifespan, consistent with myelin-
353 driven changes in volume and MRI contrast across the cortex [36]. Quantitative R1 has also shown a
354 quadratic trajectory against age indicative of region-specific myelin maturation stabilizing into
355 middle age followed by degeneration [37]. Our results indicate that age-related MT and R1 changes
356 were generally coincident, both sensitive to tissue myelin [35]. However, R1 is less sensitive to myelin
357 and reflects several physiological processes which can occur simultaneously, as modelled by its
358 linear dependency on free water, myelin, macromolecules or iron assuming a mono-exponential
359 decay [31].

360 Except for its linear increase in WM, we did not find any age-related association to PD in the
361 investigated ROIs. Across the cortex, this is consistent with Seiler et al. who reported that global
362 cortical PD did not show a significant correlation with age [38]. Looking at interregional differences
363 they detected in the temporal and occipital lobes a positive association with age. Filo et al. did not
364 find differences in macromolecular tissue volume (MTV=1-PD, non-water tissue fraction) corrected
365 for $R2^*$ in the frontal cortex, hippocampus, amygdala and frontal cortex between young adults and
366 older adults [39]. Overall, PD as a surrogate for water may be less sensitive to age-related changes of
367 tissues, although values extracted from a single ROI do not allow generalization of the results to the
368 whole cortex because of regional heterogeneity.

369 Linear and polynomial fits of $R2^*$ versus age performed significantly better on our data across ROIs
370 than exponential saturation functions as the latter could not keep up with the increase in $R2^*$ and its
371 variability in older participants. Yet early exponential growth in the putamen and caudate nucleus
372 was noticed (Sup. Fig. S7) following the putative steep iron increase from early childhood to
373 adulthood, in line with global cubic fits for the caudate, putamen, and globus pallidus reported in
374 another study [40]. Pallidal calcification was often seen in our older healthy participants, which we
375 considered as a normal aging phenomenon contributing to the $R2^*$ inter-subject variability in the
376 basal ganglia as hyperintensities may originate from the presence of minerals such as calcium and
377 zinc especially around the globus pallidus [41]. Although age-related increase in $R2^*$ has also been
378 reported for the hippocampus [42] we did not observe a dependency of $R2^*$ with age in the

379 hippocampus and thalamus, what may be a result of structural differences in rates of myelination or
380 iron accumulation [41], or due to volume shrinkage impacting iron concentration.

381 Interestingly, we noticed a concurrence between R1, MT and $R2^*$ in WM and CGM owing to their
382 sensitivity to macromolecular, myelin, iron and water content [43]. Tissue areas rich in iron often co-
383 localize with regions of elevated myelin content [44], owing to the role of iron in myelin synthesis and
384 homeostasis, or the high iron concentration within glial cells [45], adding to the dependence of $R2^*$ on
385 the orientation of WM fibers with respect to the magnetic field [46].

386 Finally, increased variability with age in $R2^*$ may partly be explained by noisier measurements given
387 the sensitivity to motion inherent to the multi-echo FLASH acquisition. As shown by the correlation
388 between age and motion degradation index, motion may also be a predictor as the ability to remain
389 still in the scanner may worsen with age. Specifically, head motion extends to the noise level of
390 relaxometry estimates derived from the raw echoes quantified by the variability of $R2^*$ in WM [47].

391 **4.3 Implications for future research and clinical practice**

392 Strengths of this study include using manufacturer sequences, which allow ready implementation on
393 standard scanners. Absolute deviations in mean or median between our MPM values across ROIs and
394 those reported in literature were in the same range as differences between previous studies
395 highlighting the reproducibility of quantitative MPM [6,7]. The prevalence and severity of WML tend
396 to rise with age with a majority of non-demented people aged above 60 exhibiting cerebral lesions [48].

397 In consideration of future research implicating WM lesions and abnormalities in multiple sclerosis
398 and related disorders, we aimed to include them in the general pipeline for lesion-filling and to
399 improve PD quantification, as i) the presence of lesions or enlarged ventricles may cause
400 segmentation to fail and ii) global effects observed in WM might transfer to lesion-specific localized
401 effects. Comparing WM and WML across MS patients and healthy participants, T2w WM
402 hyperintensities showed decreased MT, R1 and R2* and increased PD compared to healthy WM and
403 NAWM of MS indicating more pronounced focal damage and structural loss. MPM is also sensitive
404 to diffuse white matter pathology as NAWM which appears unaffected on conventional MRI can be
405 differentiated from healthy WM [49]. In particular, demyelination, axonal degeneration, inflammation,
406 gliosis and edema are exacerbated in MS plaques resulting in higher discrepancy in MPM values
407 from healthy WM and WML, corroborating findings from other studies using quantitative
408 relaxometry, MT imaging, and diffusion MRI [50]. However, MS lesions are heterogeneous and present
409 varying degrees of degeneration, de/re-myelination and inflammation, thus discriminating specific
410 lesion types remains to be explored [51,52].

411 Lastly, we hypothesized that MPM measurements might demonstrate more consistency in younger
412 healthy individuals while displaying greater variability in older populations to acknowledge the
413 impact of pre-clinical degeneration. Biological age may contribute most to the inter-subject
414 variability and even be the strongest predictor for pathophysiological changes. Early and late
415 nonlinear age-dependence have been observed in the lifespan trajectories of quantitative parameters,

with distinct patterns in MT mimicking the inverted U-shaped trajectory of human brain myelination [36] and in $R2^*$ analogous to the exponential cerebral increase of non-heme iron [53]. Yet, this relationship may be altered in disease. In multi-center or randomized clinical trials, due to discrepancy in age distribution of unmatched cohorts, including age as a linear predictor may be inadequate if one aims to fully capture the true age-related variability when manipulating biomarkers. It may be recommended to check and correct for non-linear age effects by fitting the response with age as an independent parameter. For example after fitting with an exponential saturation function, Ropele et al assessed inter-subject and inter-scanner variability of $R2^*$ and attributed large $R2^*$ variations to age suggestive of iron accumulation while scanner differences had a low impact [54].

4.4 Limitations

Although the sample size is small for robust non-linear models of age-related effects, we report healthy population MPM data which can serve as control data and such studies are scarce given the novelty of the protocol. Longitudinal studies are however superior to assess chronological pathological changes and reduce bias due to the large interindividual variability. Another liability is that the age and sex distributions of the recruited participants resemble those of typical cohorts of autoimmune neuroinflammatory diseases with a strong preponderance of women. This may however become a strength when studying such clinical populations. Indeed, our pipeline considered the inclusion of WML with MPM and is readily available for upcoming research in diseases like multiple

sclerosis and related disorders. Consequently, the recruited population did not permit to have a good representation of early and late developmental changes occurring in the brain to effectively explore the impact of aging on quantitative maps and associate it to decline in cognition or motor function. Moreover, this study was done on a white population, so our results are not necessarily applicable to other ethnicities. In this study, no visual rating of the WML was attempted as they mostly served to establish the pipeline and will be further discussed and investigated in a following study to discriminate MS specific lesions from the WM lesions described in healthy participants which are likely microangiopathic. Future developments should target improvements in both sensitivity and specificity of MRI biomarkers, as well as clinical applicability with regards to disease models.

5 Conclusion

In conclusion, we present a fast quantitative MPM pipeline at 1.6 mm isotropic resolution, which can be readily used in a clinical protocol based on manufacturer sequences, along post-processing methods including standardization of PD maps and healthy brain data acquired with it. The protocol is anticipated to possess a higher sensitivity in identifying pathological alterations in future applications in disease [12]. Importantly, previous studies [6,7], as well as the current study provide essential reference values and contribute datasets to assist clinical researchers in conducting thorough power analyses and report effect sizes that carry significance for future investigations in the context of clinical studies.

452 **Competing interests**

453 H.T is supported by iNAMES - MDC - Weizmann - Helmholtz International Research School for
454 Imaging and Data Science from NAno to MESo.

455 Q.C is supported by the Chinese Scholarship Council (CSC).

456 C.C has received research support from Novartis and Alexion and is a part of a consortium funded by
457 the U.S. Department of Defense, unrelated to this study. She also serves as a member of the Standing
458 Committee on Science for the Canadian Institutes of Health Research (CIHR).

459 D.M has received a research scholarship from the Berlin Institute of Health at Charité, Berlin,
460 Germany.

461 S.A received speaker's honoraria from Bayer, Alexion, Roche and research grants from Stiftung
462 Charité, Fritz-Thyssen-Stiftung, HEAD Genuit Stiftung, Rahel Hirsch Program, Novartis and Roche,
463 all unrelated to this study.

464 R.R. received speaking honoraria from Roche unrelated to this study.

465 M.S. has received consulting fees from Roche, Pliant therapeutics, and Octave Bioscience all
466 unrelated to this study. He is named as inventor on a patent describing use of N-acetylglucosamine as
467 myelination and immunodulating therapy.

T.S.H has received research funding from Celgene/bms and speaker honoraria from AbbVie, Bayer, and Roche both unrelated to this work.

A.U.B is cofounder and holds shares of medical technology companies Motognosis GmbH and Nocturne GmbH. He is named as inventor on several patents and patent applications describing methods for retinal image analyses, motor function analysis, multiple sclerosis serum biomarkers and myelination therapies utilizing N-glycosylation modification. He is cofounder of IMSVISUAL and has served as member of the board of directors and secretary/treasurer of IMSVISUAL. AUB is now full-time employee and holds stocks and stock options of Eli Lilly and Company. His contribution to this work is his own and does not represent a contribution from Eli Lilly.

F.P. has received research funding from Biogen, Genzyme, Guthy Jackson Foundation, Merck, Serono, Novartis, Bayer and Roche all unrelated to this work. He has received consulting fees from Alexion, Roche, Horizon, Neuraxpharm and speaker honoraria from Almirall, Bayer, Biogen, GlaxoSmithKline, Hexal, Merck, Sanofi, Genzyme, Novartis, Viela Bio, UCB, Mitsubishi Tanabe, Celgene, Guthy Jackson Foundation, Serono and Roche all unrelated to this study.

Acknowledgments

This work was supported by the Berlin Center for Advanced Neuroimaging, by iNAMES - MDC - Weizmann - Helmholtz International Research School for Imaging and Data Science from NAno to MESo, the German Research Foundation (DFG) and the Open Access Publication Fund of Charité-Universitätsmedizin Berlin. For the studies ViMS and BERLimmun, we acknowledge institutional

487 support by NCRC - Neuroscience Clinical Research Center funded by the Deutsche
488 Forschungsgemeinschaft (DFG, German Research Foundation) under Germany‘s Excellence
489 Strategy – EXC-2049–390688087 and Charité-BIH. We are thankful to our MR technicians, Cynthia
490 Kraut and Susan Pikol, for their assistance in data acquisition.

491 **Author contributions**

492 H.T: Formal analysis, Data curation, Methodology, Writing - original draft;
493 T.H: Formal analysis, Writing - review & editing;
494 Q.C.: Formal analysis, - review & editing;
495 S.H: Methodology - review & editing;
496 C.C: Data curation, review & editing;
497 P.S: Data curation, review & editing;
498 T.S.H: Data curation, review & editing;
499 S.A: Data curation, review & editing;
500 R.R: Data curation, review & editing;
501 D.M: Data curation, review & editing;
502 M.S: Data curation, review & editing;
503 L.A: Data curation, review & editing;
504 A.U.B: Conceptualization, Supervision, Writing -review and editing;

505 C.F: Data curation, Writing - review & editing;

506 F.P: Conceptualization, Supervision, Writing -review and editing

507

508 **Data availability**

509 The analysis pipeline is available at https://clinicalmpm.github.io/, including the sequence

510 configuration for Siemens PRISMA scanners. MRI data from this study cannot be shared publicly

511 due to constraints from the European General Data Protection Regulation and its implementation into

512 German laws and required consent from participants.

513

514

515 **References**

516 1 Weiskopf, N., Edwards, L. J., Helms, G., Mohammadi, S. & Kirilina, E. Quantitative
517 magnetic resonance imaging of brain anatomy and in vivo histology. *Nature Reviews Physics*
518 **3**, 570-588, doi:10.1038/s42254-021-00326-1 (2021).
519 2 Cercignani, M., Dowell, N. G. & Tofts, P. S. *Quantitative MRI of the brain: principles of*
520 *physical measurement*. (2018).
521 3 Gelman, N., Ewing, J. R., Gorell, J. M., Spickler, E. M. & Solomon, E. G. Interregional
522 variation of longitudinal relaxation rates in human brain at 3.0 T: relation to estimated iron
523 and water contents. *Magn Reson Med* **45**, 71-79, doi:10.1002/1522-
524 2594(200101)45:1<71::aid-mrm1011>3.0.co;2-2 (2001).
525 4 Schmierer, K. *et al.* Quantitative magnetization transfer imaging in postmortem multiple
526 sclerosis brain. *J Magn Reson Imaging* **26**, 41-51, doi:10.1002/jmri.20984 (2007).
527 5 Langkammer, C. *et al.* Quantitative MR imaging of brain iron: a postmortem validation study.
528 *Radiology* **257**, 455-462, doi:10.1148/radiol.10100495 (2010).
529 6 Weiskopf, N. *et al.* Quantitative multi-parameter mapping of R1, PD(*), MT, and R2(*) at
530 3T: a multi-center validation. *Front Neurosci* **7**, 95, doi:10.3389/fnins.2013.00095 (2013).

7 Leutritz, T. *et al.* Multiparameter mapping of relaxation (R1, R2*), proton density and magnetization transfer saturation at 3 T: A multicenter dual-vendor reproducibility and repeatability study. *Hum Brain Mapp* **41**, 4232-4247, doi:10.1002/hbm.25122 (2020).

8 Tabelow, K. *et al.* hMRI - A toolbox for quantitative MRI in neuroscience and clinical research. *Neuroimage* **194**, 191-210, doi:10.1016/j.neuroimage.2019.01.029 (2019).

9 Taubert, M. *et al.* Converging patterns of aging-associated brain volume loss and tissue microstructure differences. *Neurobiol Aging* **88**, 108-118, doi:10.1016/j.neurobiolaging.2020.01.006 (2020).

10 Draganski, B. *et al.* Regional specificity of MRI contrast parameter changes in normal ageing revealed by voxel-based quantification (VBQ). *Neuroimage* **55**, 1423-1434, doi:10.1016/j.neuroimage.2011.01.052 (2011).

11 Callaghan, M. F. *et al.* Widespread age-related differences in the human brain microstructure revealed by quantitative magnetic resonance imaging. *Neurobiol Aging* **35**, 1862-1872, doi:10.1016/j.neurobiolaging.2014.02.008 (2014).

12 Cooper, G. *et al.* Quantitative Multi-Parameter Mapping Optimized for the Clinical Routine. *Front Neurosci* **14**, 611194, doi:10.3389/fnins.2020.611194 (2020).

13 Harbo, H. F., Gold, R. & Tintore, M. Sex and gender issues in multiple sclerosis. *Ther Adv Neurol Disord* **6**, 237-248, doi:10.1177/1756285613488434 (2013).

14 Jarius, S. *et al.* Update on the diagnosis and treatment of neuromyelits optica spectrum disorders (NMOSD) - revised recommendations of the Neuromyelitis Optica Study Group (NEMOS). Part I: Diagnosis and differential diagnosis. *J Neurol* **270**, 3341-3368, doi:10.1007/s00415-023-11634-0 (2023).

15 Volz, S. *et al.* Quantitative proton density mapping: correcting the receiver sensitivity bias via pseudo proton densities. *Neuroimage* **63**, 540-552, doi:10.1016/j.neuroimage.2012.06.076 (2012).

16 Sperber, P. S. *et al.* Berlin Registry of Neuroimmunological entities (BERLimmun): protocol of a prospective observational study. *BMC Neurol* **22**, 479, doi:10.1186/s12883-022-02986-7 (2022).

17 Schliesseit, J., Oertel, F. C., Cooper, G., Brandt, A. U. & Bellmann-Strobl, J. Longitudinal analysis of primary and secondary factors related to fatigue in multiple sclerosis. *Acta Neurol Belg* **121**, 271-274, doi:10.1007/s13760-020-01545-6 (2021).

18 Heine, J. *et al.* Structural brain changes in patients with post-COVID fatigue: a prospective observational study. *EClinicalMedicine* **58**, 101874, doi:10.1016/j.eclinm.2023.101874 (2023).

19 Thompson, A. J. *et al.* Diagnosis of multiple sclerosis: 2017 revisions of the McDonald criteria. *Lancet Neurol* **17**, 162-173, doi:10.1016/S1474-4422(17)30470-2 (2018).

20 Helms, G., Dathe, H. & Dechent, P. Quantitative FLASH MRI at 3T using a rational approximation of the Ernst equation. *Magn Reson Med* **59**, 667-672, doi:10.1002/mrm.21542 (2008).

21 Kellner, E., Dhital, B., Kiselev, V. G. & Reisert, M. Gibbs-ringing artifact removal based on local subvoxel-shifts. *Magn Reson Med* **76**, 1574-1581, doi:10.1002/mrm.26054 (2016).

22 Lutti, A. *et al.* Restoring statistical validity in group analyses of motion-corrupted MRI data. *Hum Brain Mapp* **43**, 1973-1983, doi:10.1002/hbm.25767 (2022).

23 Tustison, N. J. *et al.* N4ITK: improved N3 bias correction. *IEEE Trans Med Imaging* **29**, 1310-1320, doi:10.1109/TMI.2010.2046908 (2010).

24 Chien, C. *et al.* Prediction of high and low disease activity in early MS patients using multiple kernel learning identifies importance of lateral ventricle intensity. *Mult Scler J Exp Transl Clin* **8**, 20552173221109770, doi:10.1177/20552173221109770 (2022).
25 Fazekas, F., Chawluk, J. B., Alavi, A., Hurtig, H. I. & Zimmerman, R. A. MR signal abnormalities at 1.5 T in Alzheimer's dementia and normal aging. *AJR Am J Roentgenol* **149**, 351-356, doi:10.2214/ajr.149.2.351 (1987).
26 van Straaten, E. C. *et al.* Impact of white matter hyperintensities scoring method on correlations with clinical data: the LADIS study. *Stroke* **37**, 836-840, doi:10.1161/01.STR.0000202585.26325.74 (2006).
27 Henschel, L. *et al.* FastSurfer - A fast and accurate deep learning based neuroimaging pipeline. *Neuroimage* **219**, 117012, doi:10.1016/j.neuroimage.2020.117012 (2020).
28 Mezer, A. *et al.* Quantifying the local tissue volume and composition in individual brains with magnetic resonance imaging. *Nat Med* **19**, 1667-1672, doi:10.1038/nm.3390 (2013).
29 Sexton, C. E. *et al.* Accelerated changes in white matter microstructure during aging: a longitudinal diffusion tensor imaging study. *J Neurosci* **34**, 15425-15436, doi:10.1523/JNEUROSCI.0203-14.2014 (2014).
30 Hegen, H., Auer, M., Zeileis, A. & Deisenhammer, F. Upper reference limits for cerebrospinal fluid total protein and albumin quotient based on a large cohort of control patients: implications for increased clinical specificity. *Clin Chem Lab Med* **54**, 285-292, doi:10.1515/cclm-2015-0253 (2016).
31 Callaghan, M. F., Helms, G., Lutti, A., Mohammadi, S. & Weiskopf, N. A general linear relaxometry model of R1 using imaging data. *Magn Reson Med* **73**, 1309-1314, doi:10.1002/mrm.25210 (2015).
32 Rooney, W. D. *et al.* Magnetic field and tissue dependencies of human brain longitudinal 1H2O relaxation in vivo. *Magn Reson Med* **57**, 308-318, doi:10.1002/mrm.21122 (2007).
33 Lorio, S. *et al.* Flexible proton density (PD) mapping using multi-contrast variable flip angle (VFA) data. *Neuroimage* **186**, 464-475, doi:10.1016/j.neuroimage.2018.11.023 (2019).
34 Weiskopf, N. *et al.* Unified segmentation based correction of R1 brain maps for RF transmit field inhomogeneities (UNICORT). *Neuroimage* **54**, 2116-2124, doi:10.1016/j.neuroimage.2010.10.023 (2011).
35 Carey, D. *et al.* Quantitative MRI provides markers of intra-, inter-regional, and age-related differences in young adult cortical microstructure. *Neuroimage* **182**, 429-440, doi:10.1016/j.neuroimage.2017.11.066 (2018).
36 Bartzokis, G. *et al.* Multimodal magnetic resonance imaging assessment of white matter aging trajectories over the lifespan of healthy individuals. *Biol Psychiatry* **72**, 1026-1034, doi:10.1016/j.biopsych.2012.07.010 (2012).
37 Yeatman, J. D., Wandell, B. A. & Mezer, A. A. Lifespan maturation and degeneration of human brain white matter. *Nat Commun* **5**, 4932, doi:10.1038/ncomms5932 (2014).
38 Seiler, A. *et al.* Multiparametric Quantitative MRI in Neurological Diseases. *Front Neurol* **12**, 640239, doi:10.3389/fneur.2021.640239 (2021).
39 Filo, S. *et al.* Disentangling molecular alterations from water-content changes in the aging human brain using quantitative MRI. *Nat Commun* **10**, 3403, doi:10.1038/s41467-019-11319-1 (2019).
40 Treit, S. *et al.* R2* and quantitative susceptibility mapping in deep gray matter of 498 healthy controls from 5 to 90 years. *Hum Brain Mapp* **42**, 4597-4610, doi:10.1002/hbm.25569 (2021).

41 Acosta-Cabronero, J., Betts, M. J., Cardenas-Blanco, A., Yang, S. & Nestor, P. J. In Vivo MRI Mapping of Brain Iron Deposition across the Adult Lifespan. *J Neurosci* **36**, 364-374, doi:10.1523/JNEUROSCI.1907-15.2016 (2016).

42 Bartzokis, G. *et al.* Brain ferritin iron may influence age- and gender-related risks of neurodegeneration. *Neurobiol Aging* **28**, 414-423, doi:10.1016/j.neurobiolaging.2006.02.005 (2007).

43 Stuber, C. *et al.* Myelin and iron concentration in the human brain: a quantitative study of MRI contrast. *Neuroimage* **93 Pt 1**, 95-106, doi:10.1016/j.neuroimage.2014.02.026 (2014).

44 Fukunaga, M. *et al.* Layer-specific variation of iron content in cerebral cortex as a source of MRI contrast. *Proc Natl Acad Sci U S A* **107**, 3834-3839, doi:10.1073/pnas.0911177107 (2010).

45 Ward, R. J., Zucca, F. A., Duyn, J. H., Crichton, R. R. & Zecca, L. The role of iron in brain ageing and neurodegenerative disorders. *Lancet Neurol* **13**, 1045-1060, doi:10.1016/S1474-4422(14)70117-6 (2014).

46 Bender, B. & Klose, U. The in vivo influence of white matter fiber orientation towards B(0) on T2* in the human brain. *NMR Biomed* **23**, 1071-1076, doi:10.1002/nbm.1534 (2010).

47 Castella, R. *et al.* Controlling motion artefact levels in MR images by suspending data acquisition during periods of head motion. *Magn Reson Med* **80**, 2415-2426, doi:10.1002/mrm.27214 (2018).

48 de Leeuw, F. E. *et al.* Hypertension and cerebral white matter lesions in a prospective cohort study. *Brain* **125**, 765-772, doi:10.1093/brain/awf077 (2002).

49 De Stefano, N. *et al.* Diffuse axonal and tissue injury in patients with multiple sclerosis with low cerebral lesion load and no disability. *Arch Neurol* **59**, 1565-1571, doi:10.1001/archneur.59.10.1565 (2002).

50 Cairns, J. *et al.* Diffusely abnormal white matter in multiple sclerosis. *J Neuroimaging* **32**, 5-16, doi:10.1111/jon.12945 (2022).

51 Rahmanzadeh, R. *et al.* A New Advanced MRI Biomarker for Remyelinated Lesions in Multiple Sclerosis. *Ann Neurol* **92**, 486-502, doi:10.1002/ana.26441 (2022).

52 Galbusera, R. *et al.* Postmortem quantitative MRI disentangles histological lesion types in multiple sclerosis. *Brain Pathol* **33**, e13136, doi:10.1111/bpa.13136 (2023).

53 Hallgren, B. & Sourander, P. The effect of age on the non-haemin iron in the human brain. *J Neurochem* **3**, 41-51, doi:10.1111/j.1471-4159.1958.tb12607.x (1958).

54 Ropele, S. *et al.* Multicenter R2* mapping in the healthy brain. *Magn Reson Med* **71**, 1103-1107, doi:10.1002/mrm.24772 (2014).

55 Lublin, F. D. *et al.* Defining the clinical course of multiple sclerosis: the 2013 revisions. *Neurology* **83**, 278-286, doi:10.1212/WNL.0000000000000560 (2014).

	MS	HC

Tables

Number of subjects [n]	27	77	
Number of subjects with cerebral WM lesions with a volume above 0.2 mL [n] (percentage)	27 (100%)	20 (26%)	
Number of T2w WM hyperintensities, mean ±SD	86.8 ± 53.7	41.9 ± 46.6	
T2w hyperintensities volume[mL], mean ±SD	21.5 ± 12.2	1.39 ± 1.63	
Age [years], mean ±SD	50 ± 9.9	42.1 ± 14.1	
Total age range [years]	26-65	20-75	
Age range for women [years]	26-65	20-75	
Age range for men [years]	44-60	22-68	
Female/male [n] (%female)	18F/9M (67%)	60F/17M (77.9%)	
Disease course, [n]	RRMS n=22 SPMS n=5	NA	
EDSS, median (IQR)	3.0 (2)	NA	
Disease duration (since symptom onset) [years], median (IQR)	15.9 (13.2)	NA	

Table 1. Demographics and clinical characteristics of the participants. MS patients were diagnosed as RRMS according to revised Mc Donald criteria[19] and as SPMS according to Lublin et al. 2014[55].

Abbreviations: HC= healthy controls, F=female, M=male, WM=white matter, SD = standard deviation, IQR = interquartile range, RRMS = relapse-remitting multiple sclerosis, SPMS = secondary progressive multiple sclerosis, EDSS = Expanded Disability Status Scale.

Parameter			MT (%)				
ROI	**WM**	**WML**	**CGM**	**DGM**	**Thalamus**	**Hippocampus**	**CSF**
Mean (SD)	1.55 (0.05)	1.24 (0.19)	0.85 (0.02)	1.05 (0.04)	1.17 (0.05)	0.83 (0.03)	0.023 (0.007)
SD over voxels	0.28	0.3	0.27	0.24	0.24	0.18	0.020
Median (IQR)	1.6 (0.06)	1.26 (0.27)	0.85 (0.03)	1.03 (0.04)	1.2 (0.07)	0.82 (0.03)	0.017 (0.008)
Intra-subject CoV (%)	18.16	25.23	31.40	22.77	20.23	21.41	89.25
Inter-subject CoV (%)	3.21	15.28	2.78	3.43	4.13	4.12	30.01
2nd - 98th Percentile	1.42 - 1.64	0.91 - 1.57	0.8 - 0.89	0.97 - 1.12	1.07 - 1.26	0.75 - 0.89	0.01 - 0.05
Min – Max (of means)	1.4 - 1.64	0.87 - 1.62	0.79 - 0.89	0.95 - 1.12	1.04 - 1.26	0.73 - 0.91	0.01 - 0.05
			PD (%)				
ROI	**WM**	**WML**	**CGM**	**DGM**	**Thalamus**	**Hippocampus**	**CSF**
Mean (SD)	69.97 (1.27)	72.91 (2.94)	78.73 (1.10)	77.37 (1.19)	76.53 (1.20)	78.9 (1.27)	100.72 (0.33)
SD over voxels	3.64	4.63	6.5	3.75	4.11	3.24	4.55
Median (IQR)	69.08 (1.84)	72.8 (4.11)	78.81 (1.36)	77.76 (2.05)	76.61 (1.78)	79.14 (1.72)	100.14 (0.23)
Intra-subject CoV	5.20	6.41	8.26	4.84	5.38	4.11	4.52
Inter-subject CoV	1.82	4.03	1.40	1.54	1.57	1.60	0.33
2nd - 98th Percentile	67.67 - 72.22	67.13 - 77.48	76.32 - 80.76	75 - 79.26	74.15 - 78.77	76.47 - 80.82	100.27 - 101.83
Min - Max	66.87 - 72.53	66.24 - 77.56	76.29 - 81.17	74.03 - 79.32	73.78 - 79.09	75.27 - 80.93	100.04 - 101.98
			R1 (s^{-1})				
ROI	**WM**	**WML**	**CGM**	**DGM**	**Thalamus**	**Hippocampus**	**CSF**
Mean (SD)	0.91 (0.03)	0.81 (0.08)	0.62 (0.01)	0.7 (0.02)	0.73 (0.02)	0.58 (0.02)	0.185 (0.005)
SD over voxels	0.12	0.13	0.1	0.11	0.09	0.07	0.016
Median (IQR)	0.92 (0.04)	0.82 (0.16)	0.61 (0.02)	0.7 (0.03)	0.73 (0.03)	0.57 (0.02)	0.186 (0.009)
Intra-subject CoV	13.62	16.64	16.34	15.59	12.84	11.25	8.71
Inter-subject CoV	2.91	9.29	2.07	2.90	3.41	2.96	2.61
2nd - 98th Percentile	0.85 - 0.96	0.7 - 0.94	0.59 - 0.64	0.67 - 0.74	0.67 - 0.77	0.55 - 0.62	0.17 - 0.19
Min - Max	0.83 - 0.96	0.7 - 0.95	0.58 - 0.64	0.66 - 0.74	0.65 - 0.78	0.54 - 0.62	0.14 - 0.20
			$R2^*$ (s^{-1})				
ROI	**WM**	**WML**	**CGM**	**DGM**	**Thalamus**	**Hippocampus**	**CSF**
Mean (SD)	21.29 (0.56)	18.99 (4.11)	18.01 (0.59)	20.89 (1.07)	20.23 (0.97)	15.92 (0.78)	2.23 (0.67)
SD over voxels	4.23	5.48	9.19	6.44	3.57	3.9	2.06
Median (IQR)	21.06 (0.87)	18.24 (2.27)	16.8 (0.78)	20.24 (1.13)	20.37 (1.09)	15.61(0.84)	1.74 (0.52)
Intra-subject CoV	19.87	25.69	51.03	30.66	17.67	24.44	90.37
Inter-subject CoV	2.64	21.61	3.30	5.11	4.80	4.92	30.03
2nd - 98th Percentile	20.4 - 22.23	15.58 - 29.6	16.96 - 18.96	19.06 - 23.32	18.4 - 22.28	14.63 - 17.71	1.39 - 5.16
Min – Max	20.11 - 22.32	15.44 - 34.94	16.78 - 19.02	18.68 - 24.12	18.27 - 22.61	14.44 - 18.97	1.32- 5.98
			Volume (mL)				
ROI	**WM**	**WML**	**CGM**	**DGM**	**Thalamus**	**Hippocampus**	**CSF**
Mean (SD)	182.15 (9.52)	1.39 (1.63)	199.85 (11.37)	15.61 (1.45)	5 (0.45)	1.05 (0.9)	18.17 (20.35)
Mean ICV (mL)			2890 (256.05)				

Table 2. Descriptive statistics for all MPM and volume measurements in white matter (WM), white matter lesions (WML), cortical grey matter (CGM), deep grey matter (DGM), thalamus,

680 hippocampus and CSF. Values are rounded at 2 decimals. Standard deviation over ROI voxels and
681 intra-subject coefficient of variation are averaged across participants. Min - Max represent minimum
682 and maximum of mean ROI values across participants. CSF values were extracted from the lateral
683 ventricles excluding voxels with T1 values lower than 4s. Please note that PD values are scaled to
684 100 p.u. normalized by the median CSF value. MT values have been linearly rescaled to reference
685 values of a MT pulse of 220° for comparison purpose to literature.

686 Abbreviations: SD standard deviation, IQR interquartile range, CoV coefficient of variation, ROI
687 region of interest, CSF cerebrospinal fluid

688

689

690

691

692

693

694

695

696

Parameter (a.u)	ROI		Coefficient β	Confidence Interval (95%)	P-value
MT (%)	**WM**		**Selected model: linear spline (F=26.18, p<0.001)**		
		Intercept	1.085	(0.911, 1.261)	<0.001
		Age (slope before 55)	-0.022	(-0.056, 0.011)	0.184
		Age (slope after 55)	-0.154	(-0.2, -0.109)	<0.001
		Normalized Volume	2.944	(1.958, 3.932)	<0.001
	CGM		**Selected model: quadratic fit (F=5.43, p=0.006)**		
		Intercept	0.846	(0.842, 0.852)	<0.001
		Age	-0.030	(-0.071, 0.011)	0.148
		Age²	-0.060	(-0.101, -0.02)	0.004
	Thalamus		**Selected model: quadratic fit (F=6.47, p<0.001)**		
		Intercept	1.011	(0.881, 1.142)	<0.001
		Normalized Volume	36.549	(10.827, 62.272)	0.006
		Age	-0.013	(-0.113, 0.088)	0.802
		Age²	-0.130	(-0.223, -0.038)	0.006
PD (%)	**WM**		**Selected model: linear fit (F=8.02, p<0.001)**		
		Intercept	76.119	(70.539, 81.701)	<0.001
		Age	0.033	(0.014, 0.054)	0.002
		Normalized Volume	-46.328	(-77.616, -15.041)	0.004
R1 (s^{-1})	**WM**		**Selected model: quadratic fit (F=15.39, p<0.001)**		
		Intercept	0.659	(0.548, 0.771)	<0.001
		Normalized Volume	1.452	(0.839, 2.064)	<0.001
		Age	-0.081	(-0.127, -0.034)	<0.001
		Age²	-0.068	(-0.115, -0.021)	0.005
	CGM		**Selected model: quadratic fit (F=4.95, p=0.01)**		
		Intercept	0.610	(0.608, 0.614)	<0.001
		Age	0.005	(-0.019, 0.029)	0.657
		Age²	-0.036	(-0.06, -0.014)	0.003
	Thalamus		**Selected model: quadratic fit (F=3.72, p=0.015)**		
		Intercept	0.667	(0.599, 0.737)	<0.001
		Age	0.008	(-0.045, 0.061)	0.760
		Age²	-0.063	(-0.111, -0.016)	0.010
		Normalized Volume	12.691	(-0.945, 26.327)	0.068
	Hippocampus		**Selected model: quadratic fit (F=3.56, p=0.018)**		
		Intercept	0.597	(0.571, 0.625)	<0.001
		Age	0.034	(0.002, 0.067)	0.038
		Age²	-0.040	(-0.072, -0.008)	0.016
		Normalized Volume	-8.598	(-18.576, 1.381)	0.090
		Sex: F vs M	-0.007	(-0.016, 0.003)	0.170
$R2^*$ (s^{-1})	**WM**		**Selected model: linear spline (F=6.50, p<0.001)**		
		Intercept	17.314	(14.905, 19.723)	<0.001
		Age (slope before 55)	0.252	(-0.22, 0.724)	0.290
		Age (slope after 55)	-0.648	(-1.22, -0.077)	0.027
		Normalized Volume	20.286	(6.687, 33.885)	0.004
	CGM		**Selected model: quadratic fit (F=10.17, p<0.001)**		
		Intercept	16.796	(16.687, 16.905)	<0.001
		Age	1.127	(0.199, 2.056)	0.018
		Age²	-1.772	(-2.702, -0.844)	<0.001

Table 3. MPM selected models in white matter (WM), cortical grey matter (CGM), thalamus and hippocampus. Normalized volume was calculated as structural volume divided by intra-cranial volume. Age coefficients estimates are given in respective parameter unit per year (a.u/y).

Figures and legends

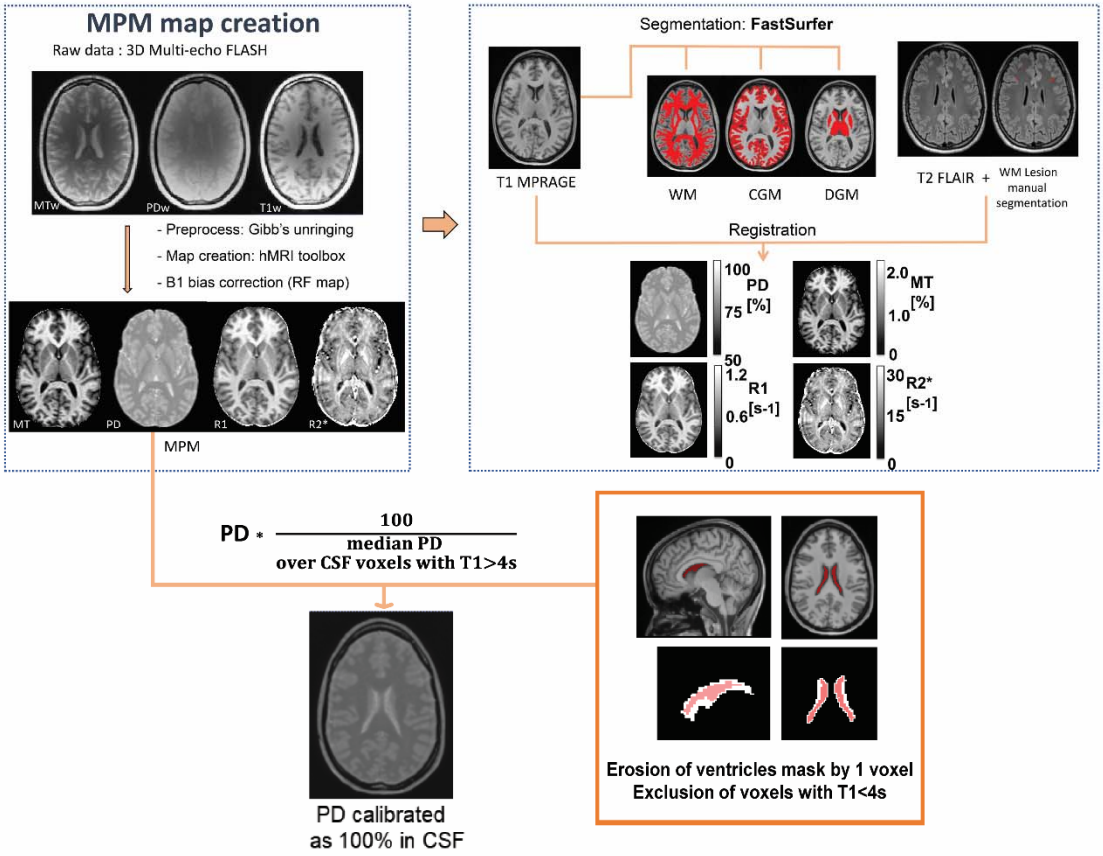

Figure 1.

Graphical representation of the MPM pipeline. Raw PDw, MTw, T1w echoes were corrected for Gibb's artifact before reconstruction with the hMRI toolbox. Receive field inhomogeneities were corrected using Unified Segmentation. T1-MPRAGE was segmented using Fastsurfer, a deep

708 learning alternative to FreeSurfer, to obtain tissue masks for white matter (WM), cortical grey matter
709 (CGM) and deep grey matter (DGM). White matter T2 hyperintensities were manually segmented
710 from T2-FLAIR. All masks were then spatially registered to the quantitative maps. PD maps were
711 calibrated as 100% in ventricular CSF. Voxels with T1<4s were excluded from the eroded lateral
712 ventricles mask.

713

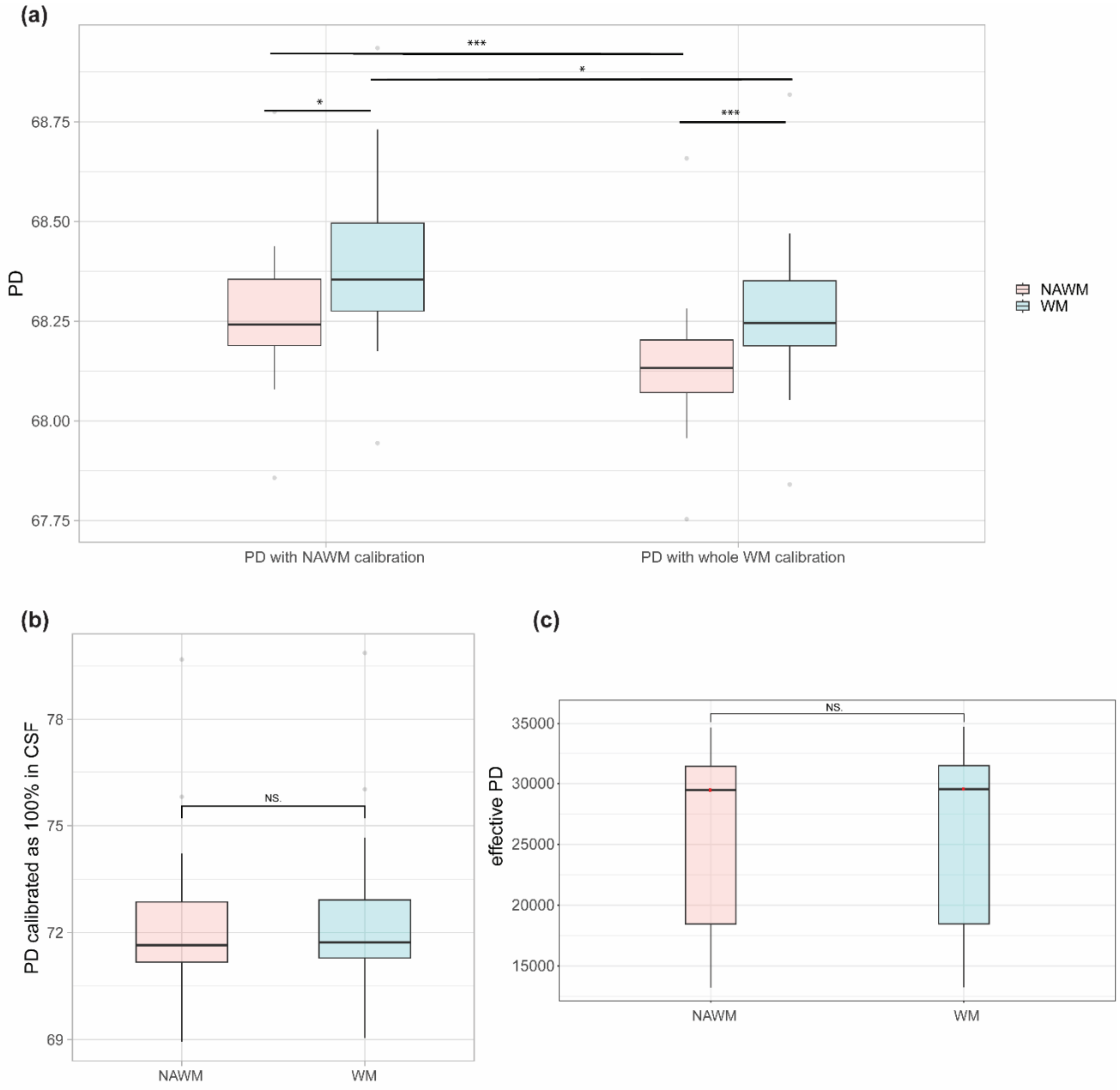

714

715 **Figure 2.**

716 **(a)** PD comparison in whole white matter (WM) and normal-appearing white matter (NAWM) of 27

717 MS patients between calibration methods using lesion-filled white matter mask (PD with NAWM

718 calibration) and whole white matter mask (PD with whole WM calibration). Significance levels
719 associated to asterisks: $p<0.05$ (*), $p<0.01$ (**), $p<0.001$ (***).

720 **(b)** Comparison of PD maps calibrated using CSF signal in normal appearing white matter (NAWM)
721 and whole white matter (WM) regions of MS patients. Using CSF calibration, the mean difference
722 between NAWM and WM is 0.1 p.u, which is of the same order of magnitude as in (a). Standard
723 deviations are higher resulting in a higher inter-subject coefficient of variation.

724 **(c)** Comparison of non-calibrated PD maps in normal appearing white matter (NAWM) and whole
725 white matter (WM) regions of MS patients

726

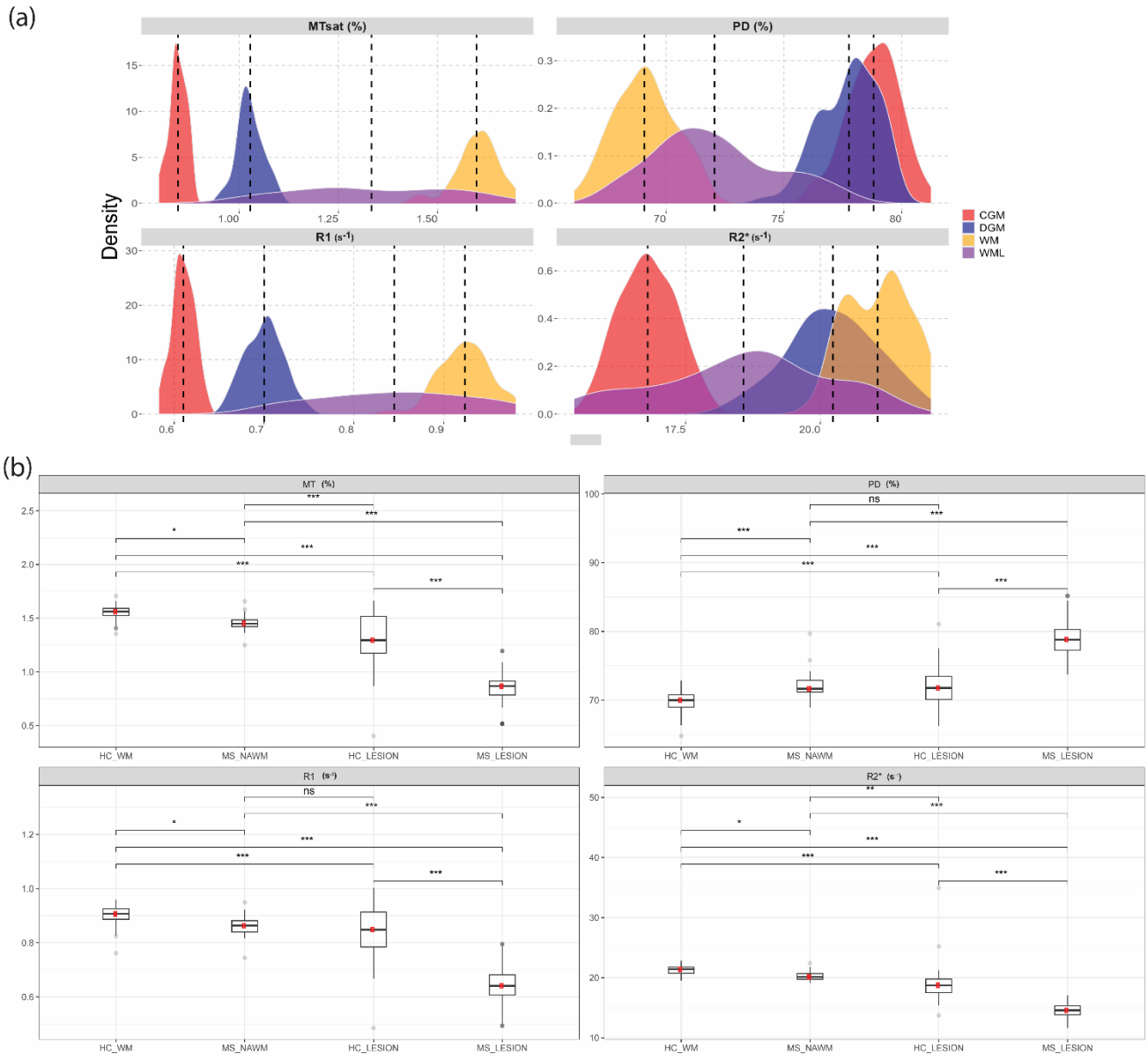

Figure 3.

(a) Histograms of median MPM values distribution across healthy participants in white matter (WM, yellow), white matter lesions (WML, purple), cortical grey matter (CGM, red), deep grey matter (DGM, blue). Dashed lines indicate respective median. For each tissue class except WML, outliers

732 outside the 2-98th percentile were removed. WML only included median values of healthy

733 participants with mean volume higher than 0.2mL.

734 **(b)** MPM comparison of white matter lesions in MS patients (MS_LESION) and HC T2w white

735 matter hyperintensities (HC_LESION) against healthy white matter (HC_WM) of healthy controls

736 and normal appearing white matter of MS patients (MS_NAWM, free of lesions). Significance levels

737 associated to asterisks: $p<0.05$ (*), $p<0.01$ (**), $p<0.001$ (***).

738

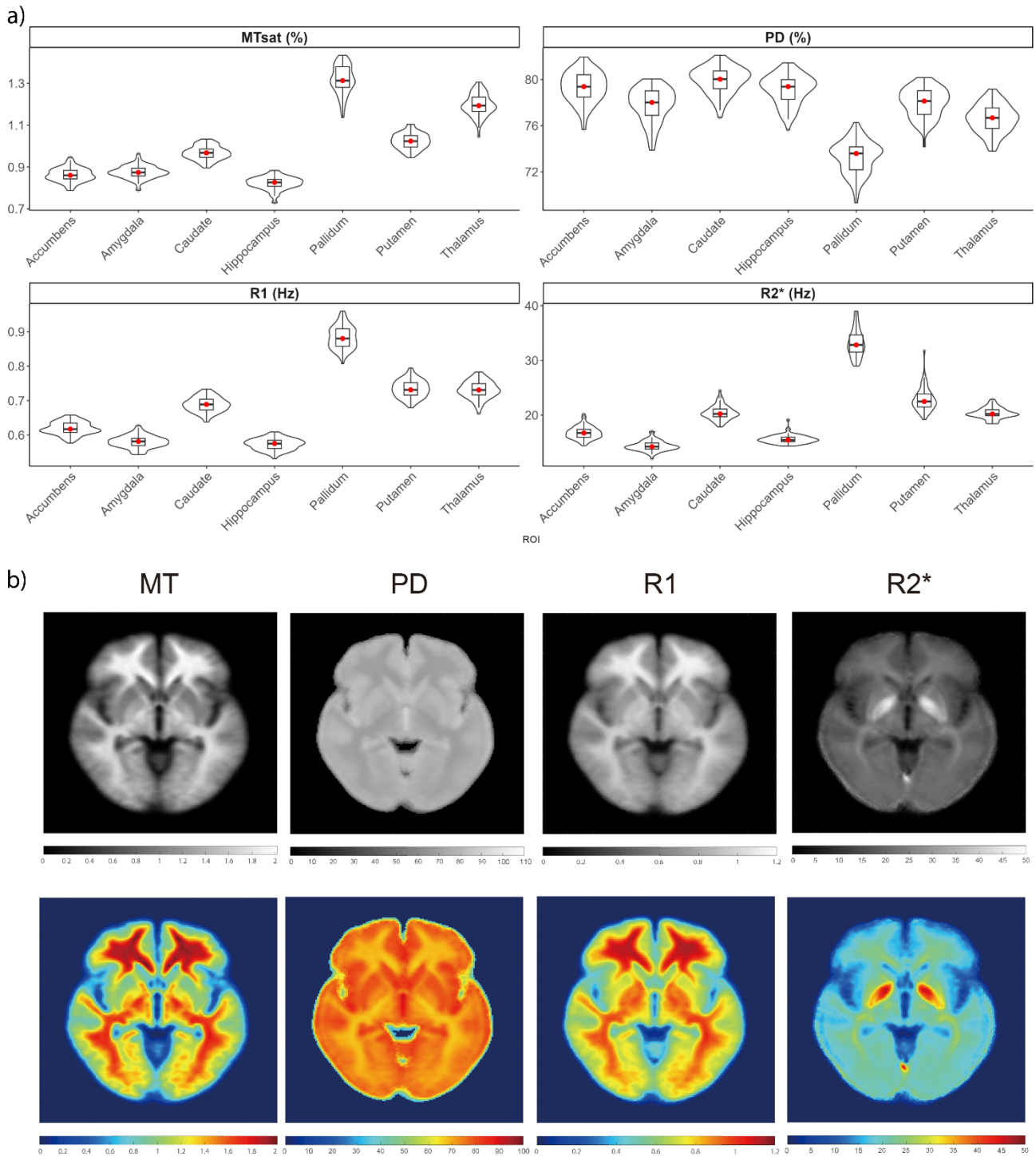

Figure 4.

741 **(a)** Boxplots and density distribution comparison of median MT, PD, R1 and $R2^*$ values in thalamus,
742 caudate, globus pallidus (Pallidum), putamen, amygdala, hippocampus, nucleus accumbens
743 (Accumbens).

744 **(b)** Greyscale and RGB-colored slice examples of population averaged quantitative maps showing
745 globus pallidus caudate putamen and thalamus. In particular, the globus pallidus shows higher $R2^*$,
746 R1, MT and lower PD values.

747

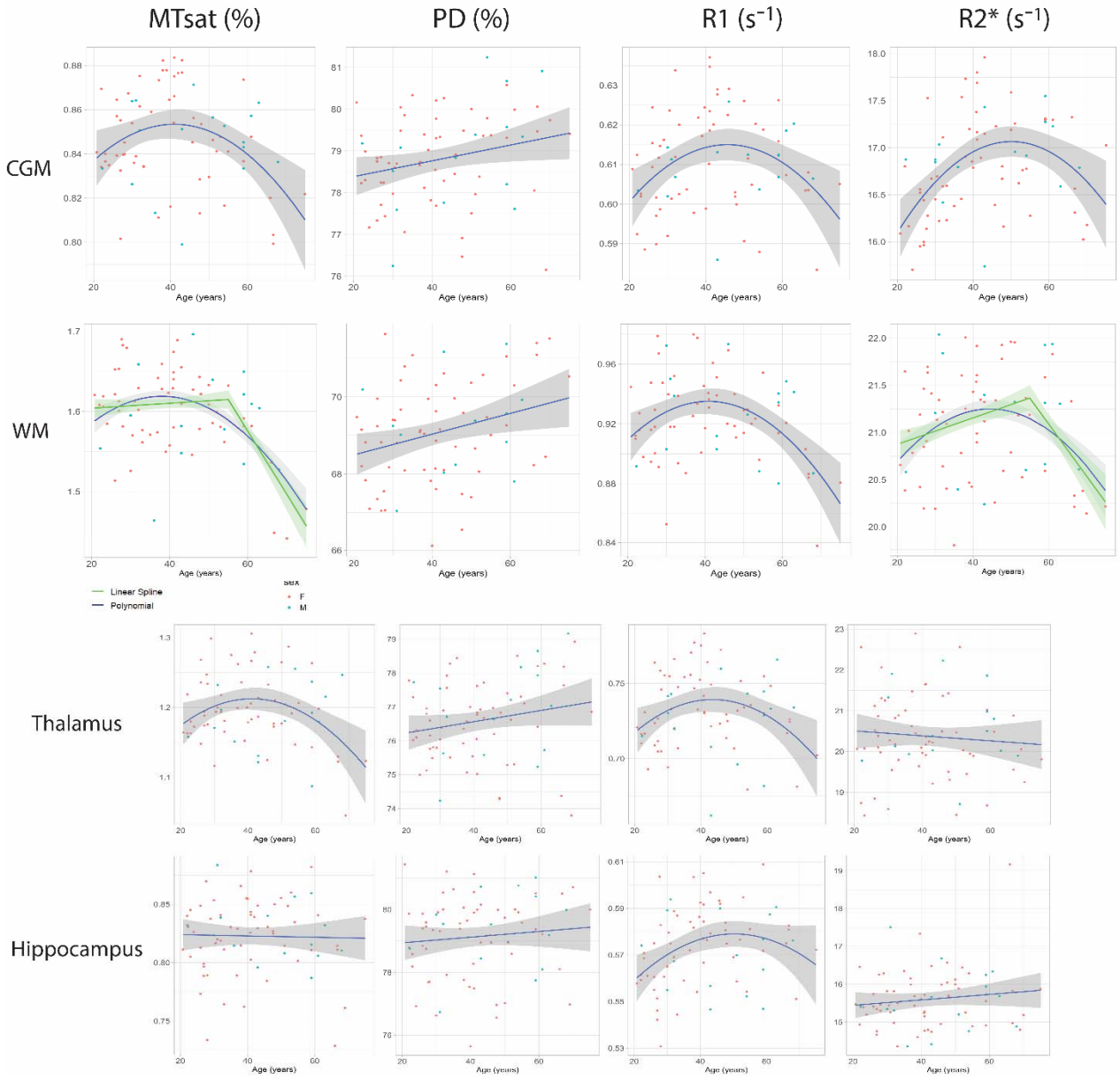

748

749 **Figure 5.** Scatterplots and fitted trajectories (blue) for the described ROIs. Green curve shows the

750 linear spline with a cut-off of 55y when it performed better than the other models. Orange curve

751 displays the cubic model which performed equally well but not significantly better than a linear

752 regression in caudate nucleus and putamen. Red and green dots represent women and men

753 respectively.